CHEMISTRY

A versatile artificial metalloenzyme scaffold enabling direct bioelectrocatalysis in solution

Xiaoti Yang[1,2], Wenjie Wu[1,2], Xiling Chen[3], Fei Wu[1,2]*, Shilong Fan[3], Ping Yu[1,2], Lanqun Mao[1,4]*

Artificial metalloenzymes (ArMs) are commonly designed with protein scaffolds containing buried coordination pockets to achieve substrate specificity and product selectivity for homogeneous reactions. However, their reactivities toward heterogeneous transformations are limited because interfacial electron transfers are hampered by the backbone shells. Here, we introduce bacterial small laccase (SLAC) as a new protein scaffold for constructing ArMs to directly catalyze electrochemical transformations. We use molecular dynamics simulation, x-ray crystallography, spectroscopy, and computation to illustrate the scaffold-directed assembly of an oxo-bridged dicobalt motif on protein surface. The resulting ArM in aqueous phase catalyzes electrochemical water oxidation without mediators or electrode modifications. Mechanistic investigation reveals the role of SLAC scaffold in defining the four-electron transfer pathway from water to oxygen. Furthermore, we demonstrate that SLAC-based ArMs implemented with Ni^{2+}, Mn^{2+}, Ru^{3+}, Pd^{2+}, or Ir^{3+} also enable direct bioelectrocatalysis of water electrolysis. Our study provides a versatile and generalizable route to complement heterogeneous repertoire of ArMs for expanded applications.

INTRODUCTION

Rapid and innovative development of artificial metalloenzymes (ArMs) with transcendental catalytic performances offers new keys for unlocking chemical reactions with no equivalent in nature. The pivotal challenge lies in harnessing desired enzymatic reactivity with manually installed metal-ligand/residue motifs. Of the undertaken metal installation strategies, ranging from non-native metal ion substitution to covalently or noncovalently anchoring metal-ligand complexes (1–6), reasonable selection of a versatile and demand-tailorable protein scaffold is always the foremost step for any implementation of designed chemistries (7–11). Recent years have received enormous implications in exploring metal-ligand/residue interactions in the internal space of proteins that confines coordination geometries, substrate entrance, and intramolecular/intermolecular electron/atom transfer and thus defines chemo-, stereo-, enantio-, or regioselectivity of homogeneous reactions (12–15). In this context, protein scaffolds with buried coordination pockets like hemoproteins have become notable choices (16). In sharp contrast to the ever-expanding homogeneous biocatalyst toolbox, the heterogeneous catalytic potential of ArMs is much less noticed, albeit being tremendous for chemical transformations involving electron or charge passage across interfaces.

One of the aspirational prospects of ArMs in the heterogeneous context is the bioelectrocatalysis for manifold applications in clean energy utilization, biofuel conversion and powering, electrosynthesis, and biosensing (17–19). Being different from homogeneous biocatalysis whereby substrates directly interact with the active sites, bioelectrocatalysis relies on distant coupling of the electrochemical-enzymatic transformations through heterogeneous electron transfer (HET) between the electrodes and catalytic metal centers. Such coupling efficiency and bioelectrocatalytic reactivity are greatly

influenced by the distance and matrix that electrons traverse. Given that a thick (>1.5 nm) insulating polypeptide shell impedes electron tunneling, the mainstream ArMs harboring backbone-shielded catalytic centers will undoubtedly face the issues of low HET efficiency and poor bioelectrocatalytic reactivity (Fig. 1A). Thus far, arduous efforts have been devoted into the electrode/enzyme interface engineering to modulate bioelectrocatalytic kinetics by either mediated or direct electron transfer (DET) strategies (17).

Outfitting ArMs with surface-confined metal centers of tunable structures, potentials, and reactivities is a straightforward path bypassing the obstacles. To construct bioelectrocatalytic ArMs capable of DET (Fig. 1A), protein scaffold with coordinating residues (e.g., histidine, cysteine, glutamate, and aspartate) located on its surface is under primary consideration. However, single or scattered surface ligating sites can hardly avoid metal ion dissociation during purification, unless stoichiometric artificial ligands are present to form metal-ligand/residue complexes (20). Abundant and centralized surface coordinating residues are beneficial for precise position and stabilization of an exposed metal moiety. Moreover, protein conformation should allow direct contact between the surface-confined metal center and electrode. In this regard, small laccase (SLAC), originated from bacteria and named because of fewer domains than fungus laccase, has attracted our attention with promises to match the stringent criteria. As a typical multicopper oxidase, SLAC owns a mononuclear Cu ion (T1 site) for phenolic substrate oxidation and a trinuclear Cu cluster (T2/T3 site) for oxygen reduction within the native dimer (21). Its uniqueness is that SLAC in the *apo* form dissociates into monomers, thus exposing a wealth of surface histidine residues. On closer inspection of the crystal structure of *apo*-SLAC resolved by Skálová *et al.* (22), two "clusters" of histidine residues located on opposite sides of the monomer represent two anchoring sites for assembling multinuclear metal centers with high exposure to solvent, ligand, and electrode as well (Fig. 1B).

Here, we take advantage of *apo*-SLAC in creating new ArMs for direct bioelectrocatalysis in no need of mediators or interface engineering. Electrochemical water oxidation is one of top energetically demanding reactions and chosen as the model reaction to certify the promises. Meanwhile, Co^{2+} ion, which provides a high potential

[1]Beijing National Laboratory for Molecular Science, Key Laboratory of Analytical Chemistry for Living Biosystems, Institute of Chemistry, Chinese Academy of Sciences, Beijing 100190, China. [2]University of Chinese Academy of Sciences, Beijing 100049, China. [3]Beijing Advanced Innovation Center for Structural Biology, School of Life Sciences, Tsinghua University, Beijing 100084, China. [4]College of Chemistry, Beijing Normal University, Beijing 100875, China.
*Corresponding author. Email: wufei317@iccas.ac.cn (F.W.); lqmao@iccas.ac.cn (L.M.)
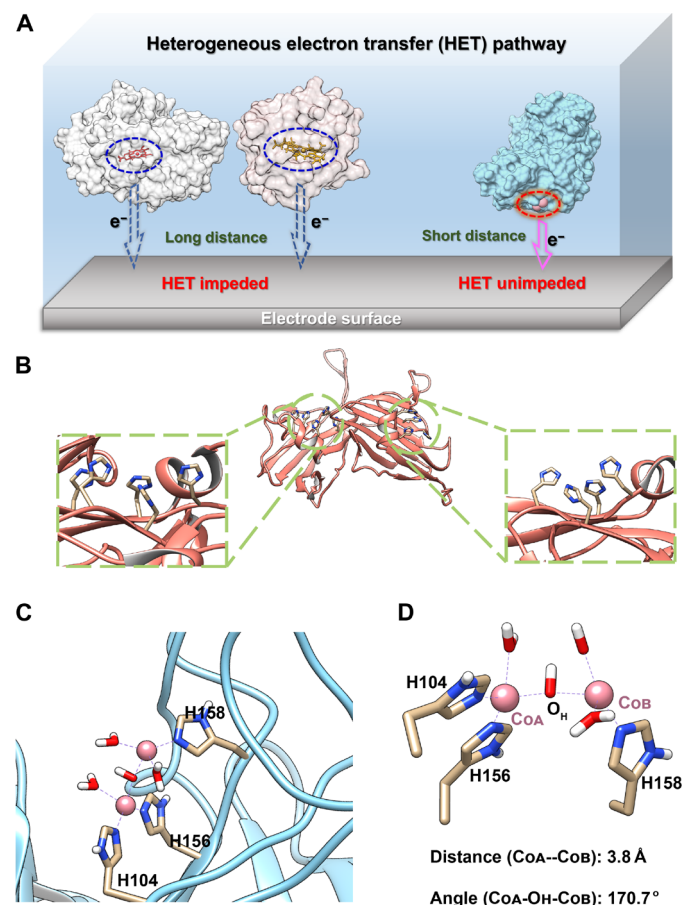
Fig. 1. Design of ArMs to enable direct bioelectrocatalysis. (**A**) Schematic of HET pathways between the electrode and ArMs with buried or exposed metal active sites. (**B**) *Apo*-SLAC monomer (PDB code, 3CG8) harboring two planarly aligned clusters of histidine residues on opposite sides, representing two potential anchoring sites for metal centers. (**C**) MD-predicted structure of an oxo-bridged dicobalt assembly with H104/H156/H158 on *apo*-SLAC monomer and three water ligands (model 1). (**D**) Zoom-in image of the simulated dicobalt assembly to illustrate the near-linear arrangement of Co_A, O_H, and Co_B. Co, N, O, and H atoms are colored in pink, blue, red, and white.

at its high-valent state to oxidize water to O_2 or H_2O_2, is adopted for configuring the catalytic center. In the present study, we demonstrate the stable, self-assembled formation of an oxo-bridged dicobalt (Co-O-Co) active center on *apo*-SLAC surface by molecular dynamics (MD) simulation, crystallography, spectroscopy, and computation. The resulting cobalt-implemented SLAC (Co-SLAC) can serve as a solubilized bioelectrocatalyst that directly promotes water oxidation and oxygen evolution reaction (OER) on unmodified electrodes at a low overpotential (1.1 V versus normal hydrogen electrode (NHE) at pH 8.0). Furthermore, we broaden the spectrum of SLAC-based ArMs featuring direct bioelectrocatalytic reactivities with Ni^{2+}, Mn^{2+}, Ru^{3+}, Pd^{2+}, and Ir^{3+}. Our work delineates the future aspiration of SLAC as a versatile scaffold for expanding the function repertoire from homogeneous to heterogeneous biocatalysis in ArM panorama.

RESULTS

### Prediction of dicobalt site formation on *apo*-SLAC surface

Investigation on the potential of *apo*-SLAC for developing bioelectrocatalytic ArMs was initiated by our query about whether an

oxo-bridged dicobalt motif (Co-O-Co), one of the classical water oxidation and OER core structures (*23*), could spontaneously form on scaffold surface through coordinating interactions between free Co^{2+} ions and histidine clusters. Given the locations of two such clusters—H102/H104/H156/H158 and H234/H236/H287/H289—we first compared the local conformations to the coordination pockets hosting oxo-bridged binuclear centers in native metalloenzymes available in Protein Data Bank (PDB). As little structural similarity was identified, the centralized histidine residues of *apo*-SLAC have their imidazole rings almost planarly aligned (fig. S1A), while native di-metal enzymes like tyrosinase show a stereo distribution of coordinating residues to accomplish the tetrahedron or octahedral geometry (fig. S1B). It could be envisaged that Co^{2+} on *apo*-SLAC would be insufficiently coordinated, which was anticipated to favor subsequent ligand binding (i.e., aqua ligands in this work) and electrochemical activation.

We then performed brief MD simulations on 5-ns time scale to assess the feasibility of *apo*-SLAC–directed dicobalt motif formation. As shown in Fig. 1C, the putative monomeric Co-SLAC model **1** has two Co^{2+} ions anchored, one (denoted as Co_A) being coordinated to two histidine residues (H104 and H156) and linked to the other (denoted as Co_B) carrying only one histidine ligand (H158) through a hydroxyl (O_H) bridge. On the basis of an initial assumption of coordination number being 4 for Co^{2+}, water molecules fill in the vacancies in the primary coordination sphere. The simulated Co_A-O_H-Co_B motif displays a distorted tetrahedron coordination geometry with an elongated Co-Co separation (3.8 Å) and unusually enlarged Co_A-O_H-Co_B angle (170.7°; Fig. 1D). Probably because of such deformation, a second Co-O-Co linkage, frequently observed in dicobalt water oxidation catalysts, is not likely to form. Notably, angles between Co-water and Co-oxo bonds rapidly decrease during initial 20-ps equilibration and then slightly fluctuate around 80° for the rest of MD run (fig. S2). Along with bond angle changes, the O-O distance between two approaching water ligands coordinated to separate Co^{2+} is shortened, which might facilitate O-O bond formation during water oxidation. Last, three more Co-SLAC forms showing different histidine linkages (**2** to **4**; fig. S3) were identified from MD simulations. In particular, model **3** coordinated to H236/H287/H289 displays merely identical core dicobalt structure and calculated energy as model **1** does, implying the possibility of forming two dicobalt centers on one *apo*-SLAC monomer or metal-mediated dimerization.

Structural elucidation of Co-O-Co motif in Co-SLAC

Incubation of recombinant *apo*-SLAC overexpressed by *Escherichia coli* with $CoCl_2$ under slightly alkaline condition [50 mM tris-HCl and 150 mM NaCl (pH 8.0)] yielded a violet-colored protein after purification (fig. S4). Our first attempt was quantifying the stoichiometric protein monomer-to-metal ratio by inductively coupled plasma mass spectroscopy (ICP-MS), which gave a ratio of 1:1.87 to affirm that each SLAC monomer did accommodate two Co^{2+} ions (fig. S5). This ratio was 1:0.19 for Zn^{2+} and 1:0.05 for Cu^{2+}, excluding the possibility of protein charging with metal ions preexisting in culture medium. To unravel accurate coordination configuration, we collected the crystal structure of Co-SLAC by x-ray diffraction (XRD) at a resolution of 2.47 Å. Figure 2A depicts the threefold symmetric Co-SLAC trimer obtained from a single cell, which formed through the "head-to-tail" assembly of monomers. An oxo-bridged dicobalt center mediated such assembly by coordinating to H104/H156/H158 on one chain, while H236/H287 on the other (Fig. 2B).
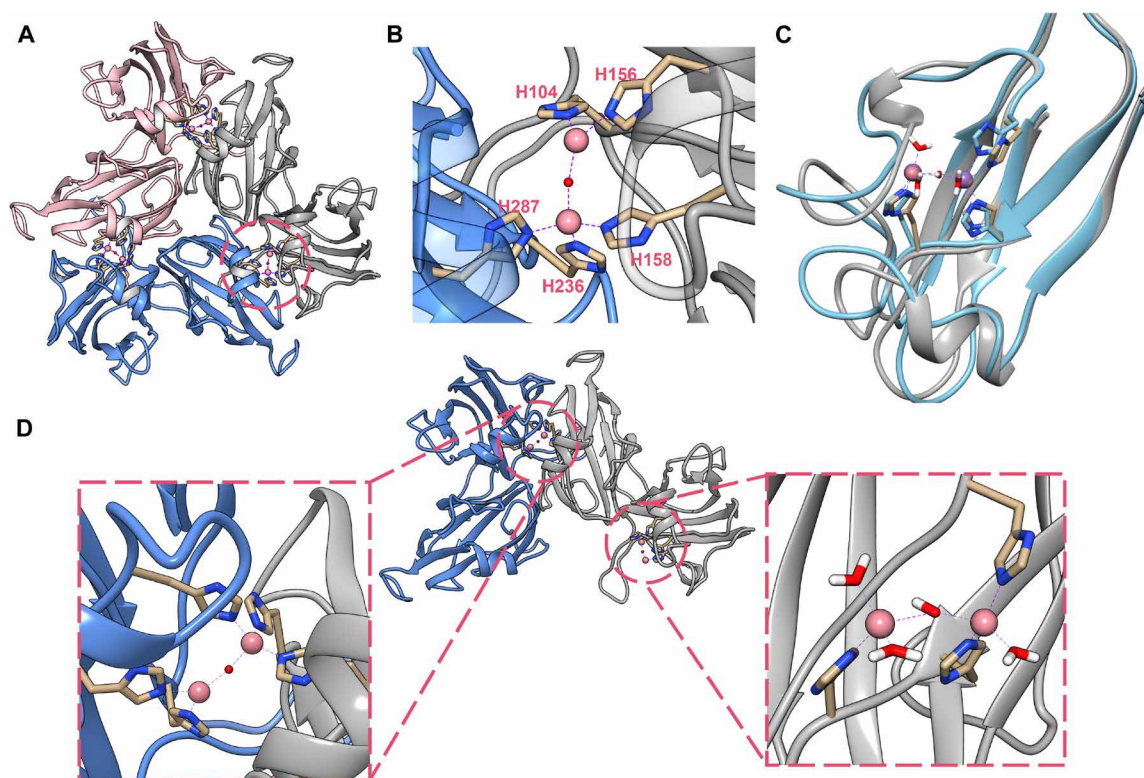
Fig. 2. Crystal structure of Co-SLAC. (**A**) The threefold symmetric Co-SLAC trimer as crystallized, formed by the head-to-tail assembly of monomers. (**B**) XRD-resolved dicobalt center stabilized by an oxo bridge and five histidine residues from two interfacing monomers. (**C**) Structural comparison of Co-bound domains obtained from crystallography (gray ribbon for backbone and pink spheres for Co atoms) and MD simulation (light blue ribbon for backbone and purple spheres for Co atoms). (**D**) Proposed asymmetric Co-SLAC dimer as solubilized in buffer solution, bearing two forms of dicobalt centers. The buried one at the subunit interface maintains the structure as crystallized, while the exposed one on the protein surface carries three water ligands to accomplish the tetrahedron coordination geometry.

Coordination number is 3 for Co_A, while it is 4 for Co_B. Aqua ligands of the Co_A-O_H-Co_B motif are missing from the crystal structure because the spatial occupation by protein residues at vacant places may exclude water molecules from binding interfaces of the trimer. We extracted the Co-bound domain of Co-SLAC monomer (L87 to L186, including the oxo-bridged cobalt atoms) and compared it with simulated models by paired chain alignment. The experimentally obtained binuclear core exhibits high structural consistency with the predicted model **1** at a root mean square deviation of 0.528 Å (Fig. 2C). The determined Co_A-O_H-Co_B angle (163°) is distinctly larger than those of naturally formed in native binuclear metalloenzymes (table S1). Unique surface residue arrangement contributes to the higher degree of geometry distortion in Co-SLAC.

Size exclusion chromatography confirmed the prevailing dimer form of Co-SLAC in aqueous solution, which sustained protein gel electrophoresis by SDS–polyacrylamide gel electrophoresis (SDS-PAGE) unless a strong denaturing pretreatment (i.e., solution boiling at 95°C for 5 min) was applied (fig. S6). ICP-MS result suggested that solubilized Co-SLAC should carry two dicobalt motifs, but symmetric assembly of a head-to-tail dimer with both binuclear sites connecting divergent subunits is not favored because of backbone rigidity (*21*). Hence, the Co-SLAC dimer must be asymmetric, bearing a surface-confined Co_A-O_H-Co_B motif and a buried one at the subunit interface (Fig. 2D). Unlike the buried metal center with restrained coordination configuration, the surface dicobalt site is insufficiently coordinated and open for interactions with water molecules. Therefore,

we proposed it as coordinated to H104/H156/H158 and three more water ligands by assigning a tetrahedron coordination geometry and divalent state to each metal center.

To validate our guess, we built a simplified metal-ligand complex **a** to represent the solvent-exposed form of dicobalt centers in Co-SLAC dimer. According to density functional theory (DFT) computation of complex **a** in various protonation/deprotonation states (fig. S7), neutral histidine side chains (imidazole rings) and the hydroxyl bridge would stabilize the surface-confined dicobalt site with the lowest energy level. The DFT-optimized complex geometry well matched the XRD-determined spatial arrangement of C, N, O_H, and Co atoms. In addition, it was found to be septet, suggesting three unpaired electrons for each Co^{2+}. The high-spin state of the surface-confined Co_A-O_H-Co_B motif was also verified by low-temperature (10 K) electron paramagnetic resonance (EPR) characterization (fig. S8).

On the ultraviolet-visible (UV-vis) absorption spectrum, the Co-SLAC dimer exhibits four distinguishable yet convoluted peaks at 525, 555, 615, and 630 nm (Fig. 3A). To explain the unusual spectroscopic behavior, we analyzed the electronic excitations of dicobalt complexes by time-dependent DFT (TD-DFT). As revealed in fig. S9, complex **a** displays a strong absorption at 665 nm due to the imidazole ligand-to-cobalt charge-transfer transition, and weaker absorption at 620 nm due to d-d transition localized on Co_A-O_H-Co_B. For complex **b** carrying more imidazole ligands (representing the buried dicobalt center), two ligand-to-metal charge transfer
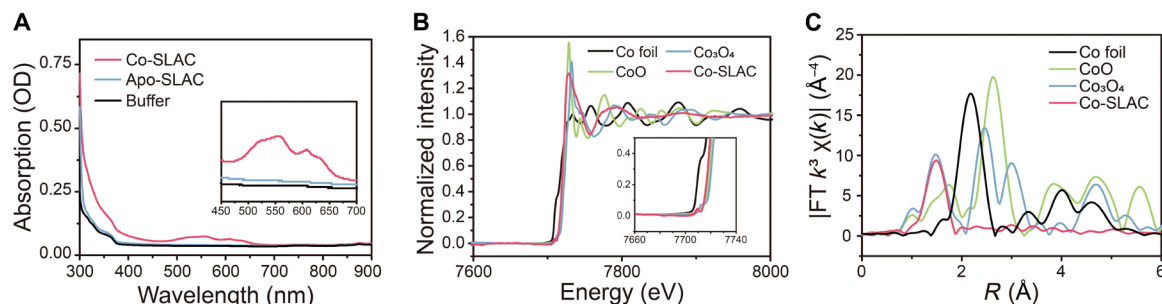
Fig. 3. Spectroscopic characterization of Co-SLAC dimer. (**A**) UV-vis absorption spectra of Co-SLAC and *apo*-SLAC solubilized in 50 mM tris-HCl buffer (150 mM NaCl, pH 8.0). Inset, zoom-in spectra from 450 and 700 nm. (**B** and **C**) Co K-edge XANES spectra (B) and Fourier-transformed (FT) k^3-weighted EXAFS spectra (C) of lyophilized Co-SLAC powder, Co foil, CoO, and Co_3O_4. Inset in (B), zoom-in spectra from 7660 to 7740 eV.

transitions at 594 and 669 nm dominate the absorption in the range of 500 to 700 nm. Furthermore, we probed the electronic and chemical environment of Co_A-O_H-Co_B motif by x-ray absorption near-edge structure (XANES) and extended x-ray absorption fine structure (EXAFS) analysis. The Co K-edge spectrum of lyophilized Co-SLAC dimer is shown in Fig. 3B and compared with the spectra of Co foil, CoO, and Co_3O_4. The protein absorption edge locates between those of Co foil and CoO while being closer to the latter, suggesting an average valence state of +2 for Co atoms in Co-SLAC. Fourier-transformed k^3-weighted EXAFS spectrum of R space for Co-SLAC exhibits only one main peak at around 1.5 Å, assigned to Co-O or Co-N coordination with no appearance of Co-Co bonding ($R > 2$ Å) in Co-SLAC (Fig. 3C). Least-squares EXAFS curve-fitting including R and k space determined the coordination number of about 4 for Co^{2+} ions (fig. S10 and table S2), indicating the presence of water ligands when Co-N coordination cannot saturate the primary shell. Together, these results finally assured the proposed configuration of the surface-confined Co_A-O_H-Co_B motif in Co-SLAC dimer.

Direct bioelectrocatalytic water oxidation by solubilized Co-SLAC

Encouraged by the experimentally solved Co-SLAC structure, we moved forward to investigate its bioelectrocatalytic reactivity toward water oxidation. Electrochemical characterization was executed in a three-electrode electrolytic setup, using a bare glassy carbon electrode (GCE; 3 mm in diameter) as working electrode. Typically, Co-SLAC or *apo*-SLAC (1 mg ml^{-1}) was dissolved in buffered electrolyte solution without any immobilization or electrode modification treatment. Cyclic voltammetry (CV) was carried out in the absence of mediators to elucidate DET behavior of solubilized enzymes (Fig. 4A) and began with measurements in slightly acidic media (pH 6.0). As compared to *apo*-SLAC, Co-SLAC produced an anodic wave onsetting at 1.1 V versus NHE with an identifiable maxima at 1.5 V, ascribed to the oxidation of $Co^{(II)}$-SLAC to catalytically active equivalent [e.g., $Co^{(III)}$-SLAC or $Co^{(IV)}$-SLAC]. The cathodic wave was hardly detected, implying that electrochemically generated high-valent dicobalt active sites were instantaneously reduced back by water molecules in the positive scan. Shifting media pH to neutral (pH 7.0) and alkaline (pH 8.0) regime further elevated the anodic current of Co-SLAC and gave rise to sigmoidal voltammograms consistent with a typical electrocatalytic water oxidation process.

During multiple scans (fig. S11), the catalytic current of water oxidation measured in Co-SLAC solution kept increasing with the number of cycles and reached a stable state after 10 cycles. In sharp

contrast, a blank solution without Co-SLAC gave a decreasing anodic current due to consumption of surface-adsorbed water molecules by consecutive oxidations. We can reason a scenario based on this phenomenon that enzyme diffusion from the bulk electrolyte solution to the GCE surface was the major mass transport–limiting factor for the catalytic current until adsorption equilibrium was established. Because the buried dicobalt conjugation with five histidine residues was strong enough to retain the dimeric form throughout SDS-PAGE, surface-adsorbed Co-SLAC dimers were not likely to dissociate into monomers under weak adsorption interactions or double-layer electric field. Electrostatic potential calculation suggested intense accumulation of negative charges near the surface-confined dicobalt center (fig. S12) to lead a fine protein orientation preferred by the DET process. To test whether the self-adsorbed Co-SLAC monolayer was stable on GCE, we rinsed the used electrodes and immersed them in quiescent buffer. CVs collected at different time points of immersion (1, 18, and 24 hours) showed continued increase of catalytic current and voltammogram transition to sigmoidal shape from that measured before electrode rinse (fig. S13). Enhancement of current intensity not only proved the stability of the protein thin film but also reflected the spontaneous reorientation of adsorbed Co-SLAC that improved its direct bioelectrocatalytic performance. The observed change in voltammogram shape indicated a transition from the enzyme transport–limiting process to the surface-limiting process.

To probe pH dependency of Co-SLAC reactivity toward water oxidation, linear sweep voltammetry (LSV) was conducted in a wider pH range of 5.0 to 10.0 (fig. S14). The polarization curves of Co-SLAC solution negatively shifted when media pH increased from 5.0 to 10.0, showing reduced activation overpotential for water oxidation relying on proton-coupled electron transfers (Fig. 4B). Once the current contribution from background water oxidation was ruled out, the largest enzyme turnover current at 1.4 V (versus NHE) was obtained at pH 8.0, which turned out to be the optimum working pH for Co-SLAC (Fig. 4C). We also noticed that an anodic peak (1.25 V versus NHE) appeared before drastic current rise on background-subtracted polarization curve collected at pH 9.0 as well as an additional peak (1.5 V versus NHE) at pH 10.0 (fig. S15). Emerging of these two peaks can be attributed to progressive oxidations of Co^{II}-SLAC to Co^{III}-SLAC and finally Co^{IV}-SLAC, providing useful clues on outlining the bioelectrocatalytic cycle.

OER activity of Co-SLAC and possible heterogeneous mechanism

Electrochemical water oxidation generally yields two products, H_2O_2 and O_2, based on whether it undergoes the two-electron or
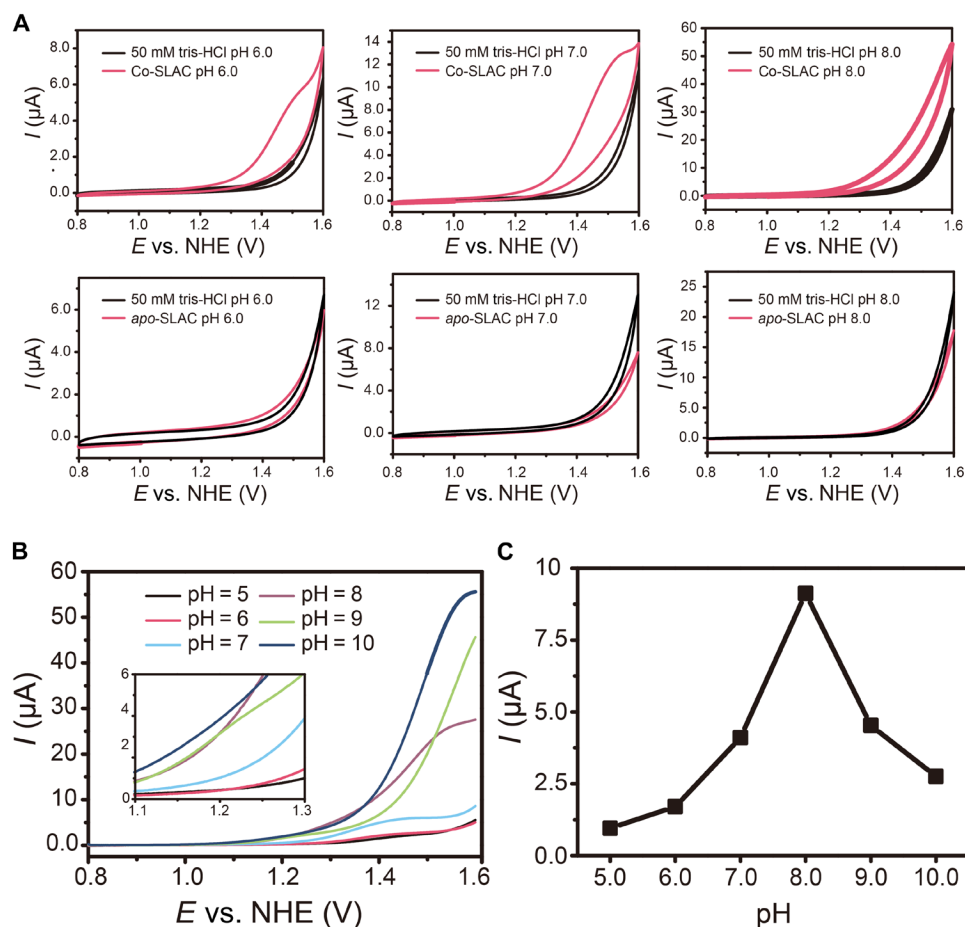
Fig. 4. Direct bioelectrocatalytic water oxidation by solubilized Co-SLAC. (**A**) CVs of Co-SLAC or *apo*-SLAC in 50 mM tris-HCl buffer (150 mM NaCl) at varying pH in a three-electrode setup. Scan rate, 10 mV s^{-1}. Working electrode, bare GCE. Counter electrode, Pt wire. Reference electrode, Ag/AgCl (saturated KCl). (**B**) LSVs of Co-SLAC in 50 mM tris-HCl buffer (150 mM NaCl) at varying pH. Inset, polarization curves in the low-overpotential range. Scan rate, 1 mV s^{-1}. (**C**) Dependence of background-subtracted oxidative current of Co-SLAC solution at 1.4 V (versus NHE) on medium pH.

four-electron pathway. To uncover the reaction pathway directed by Co-SLAC, we established an anaerobic chamber that used a squared glassy carbon slice (1.5 cm by 1.5 cm) as working electrode and an O_2 meter for monitoring O_2 evolution during bulk electrolysis. In the presence of Co-SLAC, electrolysis of a stirred slightly alkaline solution [tris-HCl buffer, 150 mM NaCl, (pH 8.0)] at 1.4 V (versus NHE) produced 0.7 part per million (ppm) dissolved O_2 in 10 min (2.1×10^{-2} μmol min^{-1}), accompanied by bubble formation on the electrode surface (Fig. 5A). Faradaic efficiency of water oxidation to O_2 was calculated as 16%. Turnover frequency was thus estimated to be 0.2 s^{-1}, almost 10 times higher than that of benchmark RuO_2 in 1 M KOH (*24*). After a 30-min electrolysis, reaction mixtures were subjected to fluorescent quantification of H_2O_2. As assayed by Amplex red kit, water oxidation in blank buffer was prevailed by the two-electron pathway on bare GCE and generated a substantial amount of H_2O_2. The presence of Co-SLAC in electrolyzed buffer, however, did not yield an increase of H_2O_2 concentration as compared to that before electrolysis (fig. S16). Blockage of GCE active sites by adsorbed enzymes prohibited H_2O_2 evolution, demonstrating Co-SLAC preference for the four-electron pathway aided by the oxo-bridged dicobalt motif.

To unravel the correlation between OER mechanism and the scaffold-defined Co_A-O_H-Co_B structure, we proceeded first with in situ Raman spectroscopic detection of OER intermediates (Fig. 5B). A sharp peak at 730 cm^{-1} attributed to Co^{IV}=O intermediate (*25*) was detected at 1.4 V and became smaller at higher potentials. In the meantime, a broad band at 325 cm^{-1} manifested itself at 1.4 V and grew with the elevation of bias potential. We assigned it to stretching and bending of a twisted Co^{III}-O-O-Co^{III} intermediate according to the DFT-calculated Raman frequency (287 and 328 cm^{-1}; fig. S17). High structural flexibility, long Co-Co separation, and hydrogen bonding interactions are probably main causes of the unexpectedly large red shift from reported values in literature (*25, 26*). Successful capture of the two species changing oppositely with positively increasing potential indicated that the rate-determining step (RDS) might be the transformation of oxo intermediate to peroxo intermediate.

Tafel analysis of OER kinetics at the electrode-enzyme interface recognized two elementary electron-transfer events with respective Tafel slope measured to be 177 and 299 mV dec^{-1}, apart from the top mass transport–limiting region (Fig. 5C). The observed Tafel slope transition when current density increased can be considered as a sign of change in surface intermediate composition and coverage
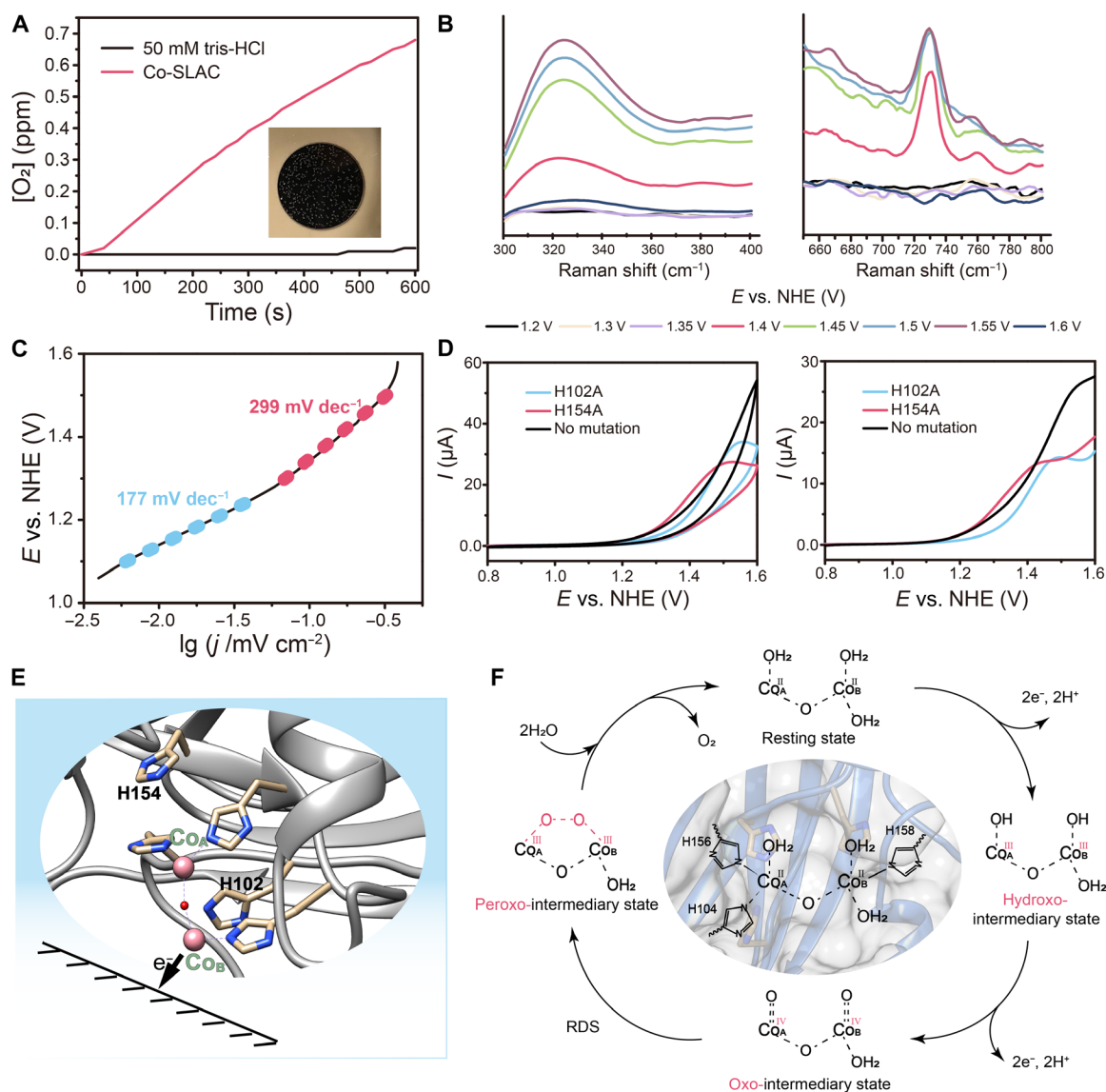
Fig. 5. Bioelectrochemical OER reactivity of Co-SLAC. (**A**) Electrochemical production of O_2 at pH 8 by bulk electrolysis at 1.4 V (versus NHE) over 10 min in the absence or presence of Co-SLAC (4 mg ml^{-1}). Working electrode, squared GC slice (1.5 cm × 1.5 cm). Inset, photo of O_2 bubble formed on bare GCE surface after electrolyzing the Co-SLAC solution. (**B**) In situ Raman spectra of Co-SLAC solution poised at different potentials. (**C**) Tafel plot of polarization curve obtained with Co-SLAC solution at pH 8.0. (**D**) CVs (left) and LSVs (right) of Co-SLAC after secondary coordination sphere mutagenesis. (**E**) Schematic of direct HET at the electrode-enzyme interface. (**F**) Proposed mechanism for Co-SLAC catalyzed oxygen-evolving water oxidation.

(27). During onset period, electrochemical oxidation of Co^{II}-OH_2 improved the fractional coverage of Co^{III}-OH intermediates. Around 1.4 V, generation of Co^{IV}=O intermediates and subsequent O-O bonding turned out to be the slower process (with increased linear slope) that dominated the overall reaction rate, which is in good agreement with Raman signatures.

Because Co_B in adsorbed Co-SLAC is closer to the electrode surface, it might be the primary electron-donating site to initiate Co_A valence change and water oxidation (Fig. 5E). However, Co_A and Co_B could share orbitals through the oxo-bridge rather than being independent atoms. To clarify the ambiguity, we exploited residues H154 and H102 in the secondary coordination sphere by site-specific single mutation. As revealed by the crystal structure of Co-SLAC,

H154 is located away from Co_A (5.0 Å) and Co_B (8.9 Å). H102 is still far from Co_B (4.5 Å) but approaches Co_A (3.7 Å) to elicit profound effects on its electron-transfer behavior. Single-site mutation of H154 to alanine did not alter the onset potential and anodic current at small overpotentials (Fig. 5D). In comparison, mutation of H102 to alanine positively shifted the onset potential as well as the whole polarization curve by about 60 mV, demonstrating synergistic participation of Co_A and Co_B in direct HET with the electrode. At large overpotentials, anodic currents of both variants drastically dropped. MD simulations found little structural change of the dicobalt motif after mutating H102 or H154 to alanine (fig. S18). The loss of OER activity might be ascribed to the electronic configuration alteration at the metal center induced by removing imidazole rings in the secondary

coordination sphere and retarded kinetics of the RDS forming the peroxo intermediate. Such electrochemical outcomes with H102A and H154A mutants not only solidify our assignment of H104, H156, and H158 as the cobalt-coordinating residues in Co-SLAC but also certify the mixed-valence nature of the surface-confined $Co_A-O_H-Co_B$ motif.

With all pieces of evidence in hand, we can deduce the complete bioelectrocatalytic cycle of Co-SLAC based on the interaction of two metal-oxo entities (I2M mechanism) (28). The heterogeneous scheme (Fig. 5F) proposes four crucial states experienced by Co-SLAC on the electrode surface: (i) the fully reduced resting state $[Co^{II}(OH_2)-O-Co^{II}(OH_2)]$ as prepared, (ii) the partially oxidized hydroxo-intermediary state $[Co^{III}(OH)-O-Co^{III}(OH)]$ formed at lower overpotential, (iii) the fully oxidized oxo-intermediary state $[Co^{IV}(=O)-O-Co^{IV}(=O)]$ formed at higher overpotential, and (iv) the peroxo-intermediary state $(Co^{III}-O-O-Co^{III})$ that ultimately releases one molecule of O_2 under the nucleophilic attack by two water molecules and returns to the resting state.

Scaffold versatility of SLAC as the bioelectrocatalytic ArM template

Having disclosed the role of SLAC scaffold in furnishing direct bio-electrocatalytic water oxidation and OER reactivity with Co^{2+}, we assessed its adaptability with more transition metals to complement heterogeneous routes. We incubated *apo*-SLAC with $NiCl_2$, $MnCl_2$, $RuCl_3$, $PdCl_2$, or $IrCl_3$ under the same condition as Co-SLAC preparation and confirmed the successful metal installation by UV-vis spectroscopy (fig. S19). Then, we conducted CV characterization of the resulting ArMs (respectively denoted as Ni-SLAC, Mn-SLAC, Ru-SLAC, Pd-SLAC, and Ir-SLAC) dissolved in the electrolyte solution at pH 7.0. As proved, all prepared SLAC-based ArMs can communicate with bare GCEs in a mediatorless manner. Mn-SLAC, Ru-SLAC, Pd-SLAC, and Ir-SLAC catalyzed the electrochemical water oxidation at the respective potential of 1.10, 1.07, 1.24, and 1.00 V when the current density reached $10\,\mu A\,cm^{-2}$ (fig. S20, A to D). Besides, to demonstrate the bioelectrocatalytic function in the negative potential range, we applied a constant positive potential (1.4 V versus NHE) to working electrode for 300 s to allow preadsorption of Ni-SLAC on bare GCE, followed by CV scans between 0.2 and −1.3 V. By this means, Ni-SLAC was able to catalyze electrochemical water (proton) reduction, with the onset potential being −0.72 V (fig. S20E). Although the crystallographic evidence is absent, DET behaviors of these ArMs on unmodified electrodes verify the formation of surface-confined metal-residue motifs.

DISCUSSION

To achieve controllable enzymatic transitions in conjunction with electrochemical techniques, the effective electrical connection of enzymes and electrodes is eagerly anticipated, which has challenged all the time owing to enzyme structure–related restrictions on HET kinetics. Motivated by the universal challenge, we have sought for new protein scaffolds to break the limit and put forward SLAC backbone as the potent candidate. We construct the prototype ArM with divalent cobalt ions for bioelectrocatalytic water oxidation and OER as the model demonstration. We illustrate the capacity of *apo*-SLAC in directing self-assembly of abiological metal active centers readily accessible by the electrode and the proceeding pathway of a complicated multistep heterogeneous transformation. Notably, the high-valent cobalt-oxo intermediate ($Co^{IV}=O$) is vulnerable to nucleophilic reagents (e.g., OH^-, NO_2^-, and R_1-S-R_2). Direct interactions between the metal-coordinated oxygen and lone electron pairs of reductants can lead to oxygen atom transfer reactions, already reported with $Fe^{IV}=O$ species on light-activated $\alpha-Fe_2O_3$, which donated oxygen atoms to different nucleophiles (29). In the present work, OER activities of Co-SLAC mutants (H102A and H154A) can be efficiently suppressed at high overpotentials, suggesting a feasible way of turning Co-SLAC into a bioelectrocatalyst for oxygenation reactions taking water molecules as both solvent and oxygen source. Furthermore, the scaffold adaptability with the first-, second-, and third-row transition metals confers function versatility on SLAC-based ArMs, not limited to water electrolysis demonstrated here.

It is appealing to bioelectrocatalyst development that a mediator-less or reagentless HET pathway can be simply established between unmodified electrodes and solubilized enzymes without any pre-treatments. As mirrored in this study, free Co-SLAC in bulk solution can adsorb on GCE surface to form an electronically coupled protein thin film. On the one hand, this behavior makes Co-SLAC as easy to handle as inorganic electrocatalysts that in situ electrochemically form active films for water oxidation (30–32), while native water-oxidizing metalloenzymes like photosystems always require sophisticated electrode modifications (33). On the other hand, we must admit that the bioelectrocatalytic reactivity of the prototype Co-SLAC is still limited by low faradaic efficiency (16%) and outperformed by many state-of-the-art synthetic OER electrocatalysts. Loss of faradaic efficiency can be ascribed to the fact that a significant portion of electrical energy goes to surmount the large mass transport resistance related with diffusional biomacromolecular catalysts. Nevertheless, biocatalytic performance of ArMs is easily optimizable in the electrochemical context, such as by electrophoretic deposition of solubilized enzymes onto electrodes before electrolysis (34, 35) or by replacing planar macroelectrodes with those featuring three-dimensional or porous morphologies to increase surface enzyme loading (36, 37).

The SLAC *apo*protein can serve as an amenable and evolvable template to create desired chemistries from diverse perspectives. First, the histidine residues on SLAC scaffold can accommodate a trinuclear metal cluster in the case of copper implementation, while a binuclear moiety in Co-SLAC. Comparing crystal structures of native SLAC and Co-SLAC, we find that $Co^{II}-N_{histidine}$ and $Cu^{II}-N_{histidine}$ are averagely 2.3 and 2.0 Å in length, suggesting a relatively stronger interaction between copper ions and histidine imidazole rings. $Co^{II}-O_H$ is 2.1 Å in length, while the average $Cu^{II}-O$ distance is 2.6 Å. We can thus speculate that stronger metal-imidazole nitrogen binding and weaker metal-oxygen binding would allow for incorporation of more metal ions that call for stabilization by divergent SLAC chains, while balanced interactions are likely to afford surface-confined metal centers stabilized by both nitrogen and oxygen ligands. In other words, it is feasible to make use of intrinsic properties of coordination bonds in predicting and shaping intended functional motifs on SLAC scaffold with different metal sources. Notably, T1 copper site (H231/C288/H293) is unoccupied in Co-SLAC, as elongated $Co^{II}-N_{histidine}$ bonds hinder the cobalt ion from fitting into the spatially restricted cavity. However, it offers the potential to establish miscellaneous multicenter ArMs with two functional metal motifs synergistically connected by the intramolecular electron-transfer (IET) pathway, which already exists to couple redox transformations at T1 site and T2/T3 site in native copper SLAC. In further steps, the highly solvent-exposed and insufficiently coordinated metal sites are

readily tunable not only by residues in the primary/secondary coordination spheres but also by synthetic ligands extensively exploited in organometallic research.

In summary, we present a new protein template for designing ArMs into competent heterogeneous tools to enable direct bioelectrocatalysis, which is out of the scope of most existing ArMs developed for homogeneous biocatalysis. Because no substrate entrance is needed, SLAC-confined surface metal active centers are expected to be promiscuous for bioelectrosynthesis applications. As we can foresee, the SLAC scaffold–based ArMs design will open up new ways to approach abiological chemical transformations with the aid of heterogeneous repertoire.

MATERIALS AND METHODS
Materials
DNA sequence encoding *Streptomyces coelicolor* SLAC was obtained from GenBank on National Center for Biotechnology Information (NCBI) databases and introduced into the *pET-20b* vector at *Nde*I and *Hind*III restriction sites after removing the signal peptide sequence. The resulting plasmid (*pET20b_SLAC*) encoded a fusion protein of *apo*-SLAC carrying a His$_6$ tag and a Tobacco Etch Virus (TEV) protease–cleavable linker (ENLYFQG) on the N terminus. For site-specific mutagenesis, SLAC gene sequence (signal peptide deleted) with single mutation (H102A or H154A) was introduced into the *pGEX-6P-1* vector at *Bam*HI and *Xho*I restriction sites. The resulting plasmids (*pGSLAC_H102A* and *pGSLAC_H154A*) encoded the SLAC mutants carrying a glutathione *S*-transferase (GST) tag and a prescission protease (PPase)–cleavable linker (LEVLFQGP) on the N terminus. All plasmids were subjected to codon optimization for *E. coli* expression system and synthesized by GenScript (Nanjing, China). Recombinant His$_6$-tagged TEV protease was purchased from Sigma-Aldrich and used without further purification. Recombinant GST-tagged PPase was purified after *E. coli* overexpression of the plasmid as a gift from M. Wang's laboratory (Institute of Chemistry, Chinese Academy of Sciences).

Protein expression and purification
To express recombinant His$_6$-tagged *apo*-SLAC, BL21(*DE3*) *E. coli* was transformed with *pET20b_SLAC* and grown on a Luria-Bertani (LB) broth agar plate containing ampicillin (100 μg ml^{-1}) at 37°C. A monoclonal colony was inoculated into 150 ml of LB broth medium containing ampicillin (100 μg ml^{-1}) and cultured overnight at 37°C (220 rpm). The cell culture was then inoculated into fresh ampicillin-supplemented (100 μg ml^{-1}) LB broth medium (1.5 liters × 8) at a volume ratio of 1:100 and grown at 37°C (220 rpm). When OD$_{600}$ (optical density at 600 nm) reached 0.6 to 0.8, isopropyl-β-D-thiogalactopyranoside (IPTG) was added to a final concentration of 0.4 mM to induce protein expression. Cells were further cultured at 25°C (220 rpm) for 18 hours and then harvested by centrifugation at 4500 rpm for 10 min. Cell pellets were resuspended in 50 mM tris-HCl buffer (pH 8.0) containing 250 mM NaCl and the protease inhibitor cocktail at a ratio of 1:10 (w/v) and disrupted by ultrasonication. Insoluble components in the cell lysate were removed by centrifugation at 12,000g, 4°C for 30 min. The clarified crude lysate was loaded onto a preequilibrated HisTrap FF Ni-NTA column by ÄKTA pure chromatography system (Cytiva) at a flow rate of 2.5 ml min^{-1} and further eluted with an imidazole gradient (0 to 500 mM) in 50 mM tris-HCl buffer (250 mM NaCl, pH 8.0). His$_6$

tag of *apo*-SLAC was removed by adding 2 mg of recombinant TEV protease per 100 mg of eluted protein, and the mixture was incubated overnight in a dialysis bag in 2 liters of 50 mM tris-HCl buffer (150 mM NaCl, pH 8.0) at 4°C. The obtained dialysate was subjected to another Ni-NTA affinity purification procedure to remove the cleaved His$_6$-tagged fragment and TEV protease and collect the untagged *apo*-SLAC in flow pass.

Expression of GST-tagged *apo*-SLAC mutants was the same as that of His$_6$-tagged *apo*-SLAC, except that BL21(*DE3*) *E. coli* was transformed with *pGSLAC_H102A* or *pGSLAC_H154A*. After cell harvest and ultrasonication, the crude lysate was loaded onto a Glutathione Sepharose 4B column by gravity, followed by a thorough wash with 50 mM tris-HCl buffer (150 mM NaCl, pH 8.0). Then, recombinant GST-tagged PPase was added onto the column with the bottom exit capped, and the mixture was stirred to ensure full contact of the protease and target proteins and allowed to settle down. After an overnight in-column incubation at 4°C, untagged *apo*-SLAC mutants were eluted out with the wash buffer and collected in flow pass.

To prepare Co-SLAC ArM, *apo*-SLAC (2 mg ml^{-1}) dissolved in 50 mM tris-HCl buffer (150 mM NaCl, pH 8.0) was incubated with 0.5 mM CoCl$_2$ at 4°C overnight under gentle shaking. Precipitates were removed by centrifugation at 12,000g for 30 min. The violet-colored supernatant was diluted with tris-HCl buffer to bring NaCl concentration down below 50 mM and then loaded onto a DEAE-Sepharose FF column at a flow rate of 2.5 ml min^{-1} for anion-exchange chromatographic purification. Co-SLAC fractions were collected with a NaCl gradient (50 to 500 mM) in 50 mM tris-HCl buffer (pH 8.0) and combined for concentrating in an Amicon centrifugal filter (30 kDa cutoff) tube (Merck Millipore). The concentrated sample was finally subjected to gel filtration through a Superdex-75 10/300 GL size exclusion column with 50 mM tris-HCl buffer (150 mM NaCl, pH 8.0) at a flow rate of 0.5 ml min^{-1}. Protein purity of each collected fraction (1 ml) was verified by SDS-PAGE. Those solely displaying Co-SLAC band were combined, concentrated, and stored in 100 μl of aliquots at −80°C for further characterizations.

Protein crystallization, data collection, and structure determination
Protein crystallization was conducted at 16°C by the sitting drop method in wells containing 100 mM Hepes (pH 7.5), 2% (v/v) polyethylene glycol 40 (PEG 40), and 2.0 M ammonium sulfate. The drops made with well solution contained Co-SLAC (40 mg ml^{-1}). The successfully grown crystals were collected and flash-frozen in liquid nitrogen for subsequent structural determination. XRD data were collected at 100 K and 2.47 Å with a complementary metal-oxide semiconductor (CMOS) detector on the BL19U beam line of the Shanghai Synchrotron Research Facility. Protein structure was built by molecular replacement with the blue copper SLAC (PDB code: 3CG8) as the starting model. Structural refinement was performed in Phenix (*38*), and model rebuilding was done in Coot (*39*). Crystallography and refinement statistics are listed in table S3.

Metal center characterization
To determine the stoichiometric protein monomer-to-metal ratio, Co-SLAC was digested in 2.0% HNO$_3$ solution at 50°C under gentle shaking for 30 min. After digestion, residual HNO$_3$ was removed by rotary evaporator. The concentrated mixture (0.5 ml) was diluted with deionized water (0.5 ml) for subsequent ICP-MS characterization using a Thermo iCAP RQ instrument. UV-vis absorption spectra of

apo-SLAC, Co-SLAC, Mn-SLAC, Ir-SLAC, Pd-SLAC, Ru-SLAC, and Ni-SLAC were collected from 300 to 800 nm on a microplate reader (BioTek Synergy H1M) or a UV-vis spectrometer (Thermo Evolution 220). EPR spectra were collected from 2500 to 4000 G at 10 K on a Bruker Elexsys E580 spectrometer. XAF characterization was performed with Si(111) crystal monochromators at the BL11B beamlines at the Shanghai Synchrotron Radiation Facility, and the spectra were collected at room temperature by four-channel silicon drift detector Bruker 5040. Under the transmission mode, the Co K-edge EXAFS spectra of Co-SLAC sample and standards (Co foil, CoO, Co_2O_3, and Co_3O_4) were obtained. Data analysis and fitting were done by the IFEFFIT software package using the Athena and Artemis modules.

Electrochemical characterization

All electrochemical measurements (CV, LSV, and bulk electrolysis) were performed in a three-electrode setup that used the bare GCE as working electrode, Pt wire as counter electrode, and Ag/AgCl in saturated KCl as reference electrode, and controlled by a 660E CHI potentiostat. Before experiments, bare GCEs or GC slices were polished with aluminum slurries (0.3 and 0.05 μm) and sonicated in ethanol and deionized water for three repeats. CV and LSV measurements were conducted in quiescent solutions at ambient conditions. Bulk electrolysis by coulometry at constant potential was conducted in a three-necked round-bottomed chamber equipped with a GC slice (1.5 cm × 1.5 cm) as the working electrode and a precalibrated dissolved oxygen meter (Mettler Toledo). Electrolytic solution was purged with high-purity Ar gas for 15 min before test to exclude predissolved O_2. During electrolysis at 1.4 V versus NHE, Ar gas stream was kept on the top of chamber to maintain the anaerobic atmosphere, and the oxygen meter immersed in the electrolytic solution was set to record a data point every 30 s over 10 min. To quantify the amount of produced H_2O_2, aliquots of the electrolytes after bulk electrolysis for 30 min were taken for Amplex red assay according to the kit protocol provided by the manufacturer. It is worth mentioning that the bulk electrolytic cell was not compartmentalized, because free proteins in the electrolyte solution would also adsorb on the Pt counter electrode and form a surface-shielding protein film suppressing O_2 or H_2O_2 reduction.

In situ Raman spectroscopy

Operando Raman spectroscopic characterization of OER intermediates was performed in a thin-layer spectroelectrochemical cell (Aida, Tianjin) using Ag/AgCl and Pt wire as the reference and counter electrodes, respectively. A detachable GCE was installed on the bottom of the cell, with the electrode surface exposed to the observation glass window on top. The height of GCE was adjusted to ensure a thin layer of electrolyte solution [50 mM tris-HCl buffer, 150 mM NaCl (pH 8.0), with or without Co-SLAC (3 mg ml^{-1})] between the working electrode surface and the sealing glass of the observation window. Before Raman sampling, the working electrode was held at a constant bias potential for 5 min to reach the steady state. All Raman spectra were collected with a Horiba LabRAM HR Evolution Raman instrument and acquired at 532-nm excitation, of which the incident power was set to 0.1% to avoid protein damage.

MD simulations

To prepare the starting structures for MD simulations of Co-SLAC, atom coordinates for *apo*-SLAC backbone were taken from PDB structure (3CG8). The oxo-bridged dicobalt structure was built using the Build Structure tool in UCSF Chimera (developed by the Resource for Biocomputing, Visualization, and Informatics at the University of California, San Francisco with support from NIH P41-GM103311) (*40*), placed nearby the coordination sites on protein backbone in a single PDB file, and restrained in a bonded mode to avoid its escape during MD simulation. Partial atomic charges were assigned to the histidine-coordinated dicobalt center based on restrained electrostatic potential calculation of complex **a** by REDS server (https://upjv.q4md-forcefieldtools.org/REDServer-Development/) (*41–43*). Initial protein structures were generated with the psfgen module in VMD (*44*) and parameterized using the CHARMM22 (*45*, *46*) force field for protein backbone and literature-derived force-field parameters (*47–49*) for the oxo-bridged dicobalt structure. Detailed information on bonded atoms, partial atomic charges, and force-field parameters of the oxo-bridged dicobalt model is provided in table S4. For MD simulations by NAMD (developed by the Theoretical and Computational Biophysics Group in the Beckman Institute for Advanced Science and Technology at the University of Illinois at Urbana-Champaign; http://www.ks.uiuc.edu/Research/namd) (*50*), enzymes were solvated in a TIP3P (*51*) water box with a distance of 15 Å to the box edge and neutralized by adding explicit Na$^+$ and Cl$^-$ ions. They were subjected to an unconstrained minimization of all atoms for geometry optimization. Equilibration was performed in an *NPT* ensemble under periodic boundary conditions at a constant pressure of 1 atm and temperature of 310 K for 5 ns with a 2-fs time step.

DFT calculations

Starting structures for complexes **a** and **b** were built using atom coordinates resolved from the crystal structure of Co-SLAC and subjected to geometry optimization and frequency calculation with Gaussian 16 (*52*), by the Perdew-Burke-Ernzerhof (PBE) functional (*53*) in combination of D3BJ dispersion correction (*54*). The LanL2DZ effective core potentials (ECP) basis set (*55*) was adopted for Co atoms and 6-31G* basis set for all nonmetal atoms (*56*). TD-DFT calculations by the PBE0 functional (*57*) were performed on the basis of the so-determined ground state geometry and were performed with a larger basis set combination, in which the def2-TZVP basis set (*58*) was used for Co and 6-311G* basis set for nonmetal atoms (*59*). Molecular orbitals inspection and visualization were conducted by the Multiwfn software (*60*).

SUPPLEMENTARY MATERIALS

REFERENCES AND NOTES

1. P. Dydio, H. M. Key, A. Nazarenko, J. Y. E. Rha, V. Seyedkazemi, D. S. Clark, J. F. Hartwig, An artificial metalloenzyme with the kinetics of native enzymes. *Science* **354**, 102–106 (2016).

2. T. K. Hyster, L. Knörr, T. R. Ward, T. Rovis, Biotinylated Rh(III) complexes in engineered streptavidin for accelerated asymmetric C-H activation. *Science* **338**, 500–503 (2012).

3. H. M. Key, P. Dydio, D. S. Clark, J. F. Hartwig, Abiological catalysis by artificial haem proteins containing noble metals in place of iron. *Nature* **534**, 534–537 (2016).

4. E. N. Mirts, I. D. Petrik, P. Hosseinzadeh, M. J. Nilges, Y. Lu, A designed heme-[4Fe-4S] metalloenzyme catalyzes sulfite reduction like the native enzyme. *Science* **361**, 1098–1101 (2018).

5. H. J. Pan, G. Huang, M. D. Wodrich, F. F. Tirani, K. Ataka, S. Shima, X. Hu, A catalytically active [Mn]-hydrogenase incorporating a non-native metal cofactor. *Nat. Chem.* **11**, 669–675 (2019).

6. S. Alonso, G. Santiago, I. Cea-Rama, L. Fernandez-Lopez, C. Coscolin, J. Modregger, A. K. Ressmann, M. Martinez-Martinez, H. Marrero, R. Bargiela, M. Pita, J. L. Gonzalez-Alfonso, M. L. Briand, D. Rojo, C. Barbas, F. J. Plou, P. N. Golyshin, P. Shahgaldian, J. Sanz-Aparicio,

V. Guallar, M. Ferrer, Genetically engineered proteins with two active sites for enhanced biocatalysis and synergistic chemo- and biocatalysis. *Nat. Catal.* **3**, 319–328 (2020).

7. U. Markel, D. F. Sauer, J. Schiffels, J. Okuda, U. Schwaneberg, Towards the evolution of artificial metalloenzymes-A protein engineer's perspective. *Angew. Chem. Int. Ed.* **58**, 4454–4464 (2019).

8. W. J. Jeong, J. Yu, W. J. Song, Proteins as diverse, efficient, and evolvable scaffolds for artificial metalloenzymes. *Chem. Commun.* **56**, 9586–9599 (2020).

9. S. Basler, S. Studer, Y. Zou, T. Mori, Y. Ota, A. Camus, H. A. Bunzel, R. C. Helgeson, K. N. Houk, G. Jimenez-Oses, D. Hilvert, Efficient Lewis acid catalysis of an abiological reaction in a de novo protein scaffold. *Nat. Chem.* **13**, 231–235 (2021).

10. G. Roelfes, LmrR: A privileged scaffold for artificial metalloenzymes. *Acc. Chem. Res.* **52**, 545–556 (2019).

11. A. Lombardi, F. Pirro, O. Maglio, M. Chino, W. F. DeGrado, De novo design of four-helix bundle metalloproteins: One scaffold, diverse reactivities. *Acc. Chem. Res.* **52**, 1148–1159 (2019).

12. C. M. Thomas, T. R. Ward, Artificial metalloenzymes: Proteins as hosts for enantioselective catalysis. *Chem. Soc. Rev.* **34**, 337–346 (2005).

13. F. Schwizer, Y. Okamoto, T. Heinisch, Y. Gu, M. M. Pellizzoni, V. Lebrun, R. Reuter, V. Kohler, J. C. Lewis, T. R. Ward, Artificial metalloenzymes: Reaction scope and optimization strategies. *Chem. Rev.* **118**, 142–231 (2018).

14. L. Falivene, Z. Cao, A. Petta, L. Serra, A. Poater, R. Oliva, V. Scarano, L. Cavallo, Towards the online computer-aided design of catalytic pockets. *Nat. Chem.* **11**, 872–879 (2019).

15. K. Chen, F. H. Arnold, Engineering new catalytic activities in enzymes. *Nat. Catal.* **3**, 203–213 (2020).

16. S. N. Natoli, J. F. Hartwig, Noble-metal substitution in hemoproteins: An emerging strategy for abiological catalysis. *Acc. Chem. Res.* **52**, 326–335 (2019).

17. H. Chen, O. Simoska, K. Lim, M. Grattieri, M. Yuan, F. Dong, Y. S. Lee, K. Beaver, S. Weliwatte, E. M. Gaffney, S. D. Minteer, Fundamentals, applications, and future directions of bioelectrocatalysis. *Chem. Rev.* **120**, 12903–12993 (2020).

18. A. Ruff, F. Conzuelo, W. Schuhmann, Bioelectrocatalysis as the basis for the design of enzyme-based biofuel cells and semi-artificial biophotoelectrodes. *Nat. Catal.* **3**, 214–224 (2020).

19. J. A. Cracknell, K. A. Vincent, F. A. Armstrong, Enzymes as working or inspirational electrocatalysts for fuel cells and electrolysis. *Chem. Rev.* **108**, 2439–2461 (2008).

20. J. J. Warren, N. Herrera, M. G. Hill, J. R. Winkler, H. B. Gray, Electron flow through nitrotyrosinate in *Pseudomonas aeruginosa* azurin. *J. Am. Chem. Soc.* **135**, 11151–11158 (2013).

21. M. C. Machczynski, E. Vijgenboom, B. Samyn, G. W. Canters, Characterization of SLAC: A small laccase from *Streptomyces coelicolor* with unprecedented activity. *Protein Sci.* **13**, 2388–2397 (2004).

22. T. Skálová, J. Dohnálek, L. H. Østergaard, P. R. Ostergaard, P. Kolenko, J. Dusková, A. Stepánková, J. Hasek, The structure of the small laccase from *Streptomyces coelicolor* reveals a link between laccases and nitrite reductases. *J. Mol. Biol.* **385**, 1165–1178 (2009).

23. N.-T. Suen, S.-F. Hung, Q. Quan, N. Zhang, Y.-J. Xu, H. M. Chen, Electrocatalysis for the oxygen evolution reaction: Recent development and future perspectives. *Chem. Soc. Rev.* **46**, 337–365 (2017).

24. X. Chen, X. Yu, Z. Yan, W. Guo, G. Fan, Y. Ni, J. Liu, W. Zhang, W. Xie, F. Cheng, J. Chen, Boosting electrocatalytic oxygen evolution by cation defect modulation via electrochemical etching. *CCS Chem.* **3**, 675–685 (2021).

25. M. Zhang, M. de Respinis, H. Frei, Time-resolved observations of water oxidation intermediates on a cobalt oxide nanoparticle catalyst. *Nat. Chem.* **6**, 362–367 (2014).

26. C. Rajani, J. R. Kincaid, D. H. Petering, Resonance Raman studies of HOO–Co(III)bleomycin and Co(III)bleomycin: Identification of two important vibrational modes, ν(Co–OOH) and ν(O–OH). *J. Am. Chem. Soc.* **126**, 3829–3836 (2004).

27. J. Zhang, H. B. Tao, M. Kuang, H. B. Yang, W. Cai, Q. Yan, Q. Mao, B. Liu, Advances in thermodynamic-kinetic model for analyzing the oxygen evolution reaction. *ACS Catal.* **10**, 8597–8610 (2020).

28. M. J. Craig, G. Coulter, E. Dolan, J. Soriano-Lopez, E. Mates-Torres, W. Schmitt, M. Garcia-Melchor, Universal scaling relations for the rational design of molecular water oxidation catalysts with near-zero overpotential. *Nat. Commun.* **10**, 4993 (2019).

29. Y. Zhao, C. Deng, D. Tang, L. Ding, Y. Zhang, H. Sheng, H. Ji, W. Song, W. Ma, C. Chen, J. Zhao, α-Fe₂O₃ as a versatile and efficient oxygen atom transfer catalyst in combination with H₂O as the oxygen source. *Nat. Catal.* **4**, 684–691 (2021).

30. M. W. Kanan, D. G. Nocera, In situ formation of an oxygen-evolving catalyst in neutral water containing phosphate and Co²⁺. *Science* **321**, 1072–1075 (2008).

31. C. C. L. McCrory, S. Jung, J. C. Peters, T. F. Jaramillo, Benchmarking heterogeneous electrocatalysts for the oxygen evolution reaction. *J. Am. Chem. Soc.* **135**, 16977–16987 (2013).

32. X. Lu, C. Zhao, Electrodeposition of hierarchically structured three-dimensional nickel-iron electrodes for efficient oxygen evolution at high current densities. *Nat. Commun.* **6**, 6616 (2015).

33. J. Z. Zhang, E. Reisner, Advancing photosystem II photoelectrochemistry for semi-artificial photosynthesis. *Nat. Rev. Chem.* **4**, 6–21 (2019).

34. M. Ammam, Electrochemical and electrophoretic deposition of enzymes: Principles, differences and application in miniaturized biosensor and biofuel cell electrodes. *Biosens. Bioelectron.* **58**, 121–131 (2014).

35. L. J. C. Jeuken, A. K. Jones, S. K. Chapman, G. Cecchini, F. A. Armstrong, Electron-transfer mechanisms through biological redox chains in multicenter enzymes. *J. Am. Chem. Soc.* **124**, 5702–5713 (2002).

36. I. Mazurenko, A. de Poulpiquet, E. Lojou, Recent developments in high surface area bioelectrodes for enzymatic fuel cells. *Curr. Opin. Electrochem.* **5**, 74–84 (2017).

37. C.-e. Zhao, P. Gai, R. Song, Y. Chen, J. Zhang, J.-J. Zhu, Nanostructured material-based biofuel cells: Recent advances and future prospects. *Chem. Soc. Rev.* **46**, 1545–1564 (2017).

38. D. Liebschner, P. V. Afonine, M. L. Baker, G. Bunkóczi, V. B. Chen, T. I. Croll, B. Hintze, L. W. Hung, S. Jain, A. J. McCoy, N. W. Moriarty, R. D. Oeffner, B. K. Poon, M. G. Prisant, R. J. Read, J. S. Richardson, D. C. Richardson, M. D. Sammito, O. V. Sobolev, D. H. Stockwell, T. C. Terwilliger, A. G. Urzhumtsev, L. L. Videau, C. J. Williams, P. D. Adams, Macromolecular structure determination using x-rays, neutrons and electrons: Recent developments in phenix. *Acta Crystallogr. D Struct. Biol.* **75** (Pt. 10), 861–877 (2019).

39. P. Emsley, B. Lohkamp, W. G. Scott, K. Cowtan, Features and development of *Coot*. *Acta Crystallogr.* **66** (Pt. 4), 486–501 (2010).

40. E. F. Pettersen, T. D. Goddard, C. C. Huang, G. S. Couch, D. M. Greenblatt, E. C. Meng, T. E. Ferrin, UCSF chimera—A visualization system for exploratory research and analysis. *J. Comput. Chem.* **25**, 1605–1612 (2004).

41. F.-Y. Dupradeau, A. Pigache, T. Zaffran, C. Savineau, R. Lelong, N. Grivel, D. Lelong, W. Rosanski, P. Cieplak, The R.E.D. tools: Advances in RESP and ESP charge derivation and force field library building. *Phys. Chem. Chem. Phys.* **12**, 7821–7839 (2010).

42. E. Vanquelef, S. Simon, G. Marquant, E. Garcia, G. Klimerak, J. C. Delepine, P. Cieplak, F.-Y. Dupradeau, R.E.D. server: A web service for deriving RESP and ESP charges and building force field libraries for new molecules and molecular fragments. *Nucl. Acids Res.* **39**, W511–W517 (2011).

43. C. I. Bayly, P. Cieplak, W. Cornell, P. A. Kollman, A well-behaved electrostatic potential based method using charge restraints for deriving atomic charges: The RESP model. *J. Phys. Chem.* **97**, 10269–10280 (1993).

44. W. Humphrey, A. Dalke, K. Schulten, VMD: Visual molecular dynamics. *J. Mol. Graph.* **14**, 33–38 (1996).

45. A. D. MacKerell Jr., D. Bashford, M. Bellott, R. L. Dunbrack Jr., J. D. Evanseck, M. J. Field, S. Fischer, J. Gao, H. Guo, S. Ha, D. Joseph-McCarthy, L. Kuchnir, K. Kuczera, F. T. K. Lau, C. Mattos, S. Michnick, T. Ngo, D. T. Nguyen, B. Prodhom, W. E. Reiher III, B. Roux, M. Schlenkrich, J. C. Smith, R. Stote, J. Straub, M. Watanabe, J. Wiórkiewicz-Kuczera, D. Yin, M. Karplus, All-atom empirical potential for molecular modeling and dynamics studies of proteins. *J. Phys. Chem. B* **102**, 3586–3616 (1998).

46. A. D. MacKerell Jr., M. Feig, C. L. Brooks III, Extending the treatment of backbone energetics in protein force fields: Limitations of gas-phase quantum mechanics in reproducing protein conformational distributions in molecular dynamics simulations. *J. Comput. Chem.* **26**, 1400–1415 (2004).

47. S. Adam, M. Knapp-Mohammady, J. Yi, A.-N. Bondar, Revised CHARMM force field parameters for iron-containing cofactors of photosystem II. *J. Comput. Chem.* **39**, 7–20 (2018).

48. A. Pavlova, J. M. Parks, J. C. Gumbart, Development of CHARMM-compatible force-field parameters for cobalamin and related cofactors from quantum mechanical calculations. *J. Chem. Theory Comput.* **14**, 784–798 (2018).

49. D. Kuter, V. Streltsov, N. Davydova, G. A. Venter, K. J. Naidoo, T. J. Egan, Molecular structures and solvation of free monomeric and dimeric ferriheme in aqueous solution: Insights from molecular dynamics simulations and extended x-ray absorption fine structure spectroscopy. *Inorg. Chem.* **53**, 10811–10824 (2014).

50. J. C. Phillips, D. J. Hardy, J. D. C. Maia, J. E. Stone, J. V. Ribeiro, R. C. Bernardi, R. Buch, G. Fiorin, J. Henin, W. Jiang, R. McGreevy, M. C. R. Melo, B. K. Radak, R. D. Skeel, A. Singharoy, Y. Wang, B. Roux, A. Aksimentiev, Z. Luthey-Schulten, L. V. Kale, K. Schulten, C. Chipot, E. Tajkhorshid, Scalable molecular dynamics on CPU and GPU architectures with NAMD. *J. Chem. Phys.* **153**, 044130 (2020).

51. W. L. Jorgensen, J. Chandrasekhar, J. D. Madura, R. W. Impey, M. L. Klein, Comparison of simple potential functions for simulating liquid water. *J. Chem. Phys.* **79**, 926–935 (1983).

52. M. J. Frisch, G. W. Trucks, H. B. Schlegel, G. E. Scuseria, M. A. Robb, J. R. Cheeseman, G. Scalmani, V. Barone, G. A. Petersson, H. Nakatsuji, X. Li, M. Caricato, A. V. Marenich, J. Bloino, B. G. Janesko, R. Gomperts, B. Mennucci, H. P. Hratchian, J. V. Ortiz, A. F. Izmaylov, J. L. Sonnenberg, D. Williams-Young, F. Ding, F. Lipparini, F. Egidi, J. Goings, B. Peng, A. Petrone, T. Henderson, D. Ranasinghe, V. G. Zakrzewski, J. Gao, N. Rega, G. Zheng, W. Liang, M. Hada, M. Ehara, K. Toyota, R. Fukuda, J. Hasegawa, M. Ishida, T. Nakajima, Y. Honda, O. Kitao, H. Nakai, T. Vreven, K. Throssell, J. A. M. Jr., J. E. Peralta, F. Ogliaro, M. J. Bearpark, J. J. Heyd, E. N. Brothers, K. N. Kudin, V. N. Staroverov, T. A. Keith, R. Kobayashi, J. Normand, K. Raghavachari, A. P. Rendell, J. C. Burant, S. S. Iyengar,

J. Tomasi, M. Cossi, J. M. Millam, M. Klene, C. Adamo, R. Cammi, J. W. Ochterski, R. L. Martin, K. Morokuma, O. Farkas, J. B. Foresman, D. J. Fox, in *Gaussian 16 Revision C.01* (Gaussian Inc., 2016).

53. J. P. Perdew, K. Burke, M. Ernzerhof, Generalized gradient approximation made simple. *Phys. Rev. Lett.* **77**, 3865–3868 (1996).

54. S. Grimme, J. Antony, S. Ehrlich, H. Krieg, A consistent and accurate *ab initio* parametrization of density functional dispersion correction (DFT-D) for the 94 elements H-Pu. *J. Chem. Phys.* **132**, 154104 (2010).

55. P. J. Hay, W. R. Wadt, *Ab initio* effective core potentials for molecular calculations. Potentials for K to Au including the outermost core orbitals. *J. Chem. Phys.* **82**, 299–310 (1985).

56. W. J. Hehre, R. Ditchfield, J. A. Pople, Self-consistent molecular orbital methods. XII. Further extensions of Gaussian-type basis sets for use in molecular orbital studies of organic molecules. *J. Chem. Phys.* **56**, 2257–2261 (1972).

57. C. Adamo, V. Barone, Toward reliable density functional methods without adjustable parameters: The PBE0 model. *J. Chem. Phys.* **110**, 6158–6170 (1999).

58. F. Weigend, R. Ahlrichs, Balanced basis sets of split valence, triple zeta valence and quadruple zeta valence quality for H to Rn: Design and assessment of accuracy. *Phys. Chem. Chem. Phys.* **7**, 3297–3305 (2005).

59. R. Krishnan, J. S. Binkley, R. Seeger, J. A. Pople, Self-consistent molecular orbital methods. XX. A basis set for correlated wave functions. *J. Chem. Phys.* **72**, 650–654 (1980).

60. T. Lu, F. Chen, Multiwfn: A multifunctional wavefunction analyzer. *J. Comput. Chem.* **33**, 580–592 (2012).